High performance hybrid supercapacitor device based on cobalt manganese layered double hydroxide and activated carbon derived from cork (Quercus Suber)

F. O. Ochai-Ejeh, M. J. Madito, D. Y. Momodu, A. A Khaleed, O. Olaniyan, N. Manyala*

Department of Physics, Institute of Applied Materials, SARChI Chair in Carbon Technology and Materials, University of Pretoria 0028, South Africa.

*Corresponding author's email: ncholu.manyala@up.ac.za, Tel.: + (27)12 420 3549;

Fax: + (27)12 420 2516

Highlights

• Thin Co-Mn LDH nanoflakes was synthesized by a facile solvothermal technique.
• AC was synthesized by a two-step eco-friendly hydrothermal synthesis.
• A device was fabricated using Co-Mn LDH as positive and AC as negative electrode.
• The electrode materials exhibited good electrochemical performance.

ABSTRACT

Thin Co-Mn layered double hydroxide (LDH) nanoflakes and Activated carbon (AC) from cork raw material (Quercus Suber) with highly porous structure and good textural properties was synthesized by a facile solvothermal and two-step eco-friendly hydrothermal syntheses routes respectively. A hybrid device was successfully fabricated using Co-Mn LDH as the positive electrode and AC as negative electrode. The device exhibited a high energy density of 20.3 W h kg^{-1} and corresponding power density of up to 435 W kg^{-1} at 0.5 A g^{-1} current density in 1 M KOH aqueous electrolyte. The device also displayed a very high stability with 99.7% capacitance retention after 10,000 continuous charge-discharge cycles and negligible degradation after subsequently subjecting it to voltage holding test at its maximum

operating voltage for 70 hours. These results showcase the potential use of this hybrid device as possible electrodes for high energy density supercapacitor application.

KEYWORDS: Supercapacitor; Hybrid device; Activated Carbon; Solvothermal; Cobalt manganese LDH

Graphical abstract
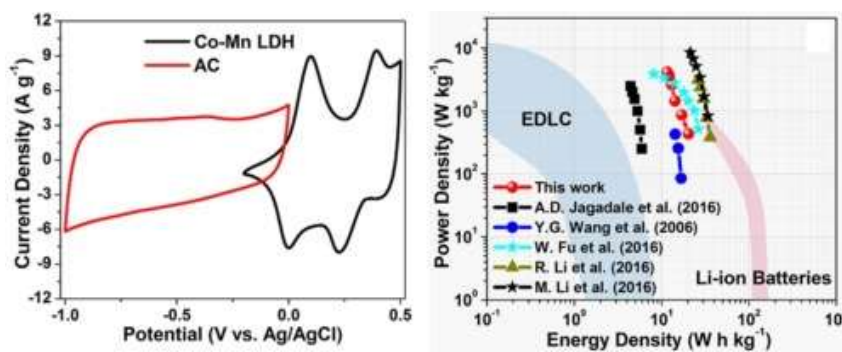
1. INTRODUCTION

Supercapacitors (SCs) are highly desirable as energy storage devices because they have the merit of being low cost, with high power density, excellent reversibility, good stability and fast charge - discharge propagation [1–3]. As compared to electrolytic and electrostatic capacitors, SCs have higher energy density but they are still reasonably lower than batteries and fuel cells. This limits their use to supply energy for extended periods of time except when they are combined with lithium-ion batteries or some other power sources [2,4]. This has stimulated the research interest on the energy density of SCs to be comparable to that of batteries. Based on the mechanism of charge, SCs can be grouped into three categories

namely, electric double layer capacitors (EDLCs), faradaic capacitors or pseudocapacitors. EDLCs store energy by a non-faradaic process which involves electrostatic reversible absorption or desorption of ions at the interface of the electrode/electrolyte. Faradaic capacitors store charges through rapid redox reaction involving intercalation of ions at the active material surface. While pseudocapacitors, store charges through an electron transfer mechanism rather than by just the accumulation of ions on the electrochemical double layer [4,5][6][7]. Hybrid supercapacitors often make use of both EDLC and faradaic type storage mechanism by combining the individual characteristics of the faradaic and non-faradaic capacitors so as to optimize their energy without losing the power density [4,8,9].

Several types of EDLC materials have been utilized as SCs material electrodes. These includes carbide-derived carbons, graphene, carbon-nanofibers, zeolite-templated carbon, carbon nanotubes (CNTs) and activated carbon [10–22]. Amongst these materials, the most commonly used in hybrid devices is activated carbon due to its high specific surface area (SSA), ease of production, light weight, relatively low cost, good porosity and presence of pseudocapacitive charge transfer mechanism which can contribute to increased specific capacitance due to the presence of functional groups [3,8,23–25]. However, controlling the pore structure has not been that easy to achieve despite extensive research and improvement on the activation process and this greatly limits their performance in some applications [13,24,26]. This is because supercapacitors require a good combination of a hierarchical pore size distribution with large SSA for optimal performance [27,28]. In the production of porous carbons, KOH has been the most common chemical activating agent, but its corrosiveness and environmental unfriendliness limits its industrial utilization [27,28].The poor textural and morphological properties recorded from many carbon-containing precursors including some biomass materials, have also hampered on the

efficient device application of activated carbon [24,27,29]. Recently, hydrochar has been considered a better precursor for the synthesis of high performance carbons since they have a high concentration of oxygenated functional groups[27,29–31]. In addition to pre-treatment of the carbon containing sources, some studies have also adopted other types of activating agents for the synthesis of porous carbons with good porosity and high surface areas [23,27–29]. Amongst these, potassium bi-carbonate (K_2CO_3) and potassium hydrogen carbonate ($KHCO_3$), have been recently shown to preserve the hydrochar morphology due to its mild nature as compared to KOH, leading to production of activated carbons with closely packed porous structures with lesser ion diffusion distances resulting in better electrochemical performance [23]. Potassium-based activating agents easily operate independent of the ordering of the material structure which makes the K-intercalation easily attainable [30]. Various materials have also been used as positive electrode materials for hybrid SC devices. These includes conducting polymers, metal oxides, metal hydroxides and bi-metallic hydroxides [31–33] because they offer good redox activity, are relatively cheap, easily produced with facile synthesis techniques, have low toxicity and are environmentally friendly [33,34].

Metal layered double hydroxides (LDH) have been reported to have higher conductivity, large inter-layer spacing, better ion exchange and transport for the reaction species which are neccessary for the production of hybrid devices with superior electrochemical performance [35–37]. Some of the LDH materials that have been investigated as positive electrode materials for hybrid supercapacitors include Ni-Co, Co-Al, Ni-Al, Ni-Mn, Co-Mn etc [41–44]. More specifically, Co-Mn has recently attracted research interest due to the unique redox combination of both Co^{2+}/Mn^{2+} and many researchers have reported on optimizing the structure and morphology of the as-synthesized Co-Mn LDH and its composites with

other materials using various interesting techniques. Nonetheless, they are still quite limited studies which have been actively carried out on the electrochemical evaluation of the Co-Mn LDH material using it as a positive electrode material with activated carbon from cheap biomass sources as the negative electrode for high energy density hybrid supercapacitors. Furthermore, only a few studies actually exist on studying the device stability of this particular hybrid combination with respect to actual testing conditions suitable for practical use.

The present report, embarks on a detailed evaluation of the electrochemical performance of a hybrid electrochemical capacitor consisting of nanostructured Co-Mn LDH as positive electrode and activated carbon as negative electrode. The full device after being subjected to the routine electrochemical tests was also exposed to lengthy floating and self-discharge tests to fully elucidate the processes taking place at the electrode/electrolyte level. The results obtained from this study would aid in the further understanding of the processes which occur after a maximum voltage has been applied over a long period of time and this would lead to developing novel blueprints for designing stable and efficient hybrid energy storage devices.

2. EXPERIMENTAL

2.1 Material synthesis

Synthesis of Co-Mn LDH (Positive electrode material)

CH_4N_2O (Merck, Purity ≥ 98 %), $Co(NO_3)2.6H_2O$ (Sigma Aldrich ≥ 98 %), $MnSO_4.H_2O$ (Merck, Purity ≥ 98 %) and CH_3OH (Sigma Aldrich ≥ 99.9 %) were used without further purification.

Co-Mn LDH nanoflakes was synthesized by a facile solvothermal method. In a typical synthesis procedure, 0.05 M $Co(NO_3)_2.6H_2O$, 0.10 M $MnSO_4.H_2O$ and 0.60 M CH_4N_2O was put into 60 ml of methanol (CH_3OH) and sonicated for 10 minutes. The solution was then poured into a 100 ml Teflon lined autoclave and placed in the oven at 120 °C for 6 hours. The resulting product was then filtered and washed several times with deionized water. Scheme 1 shows the complete synthesis route of the Co-Mn LDH nanoflakes (see micrograph image).
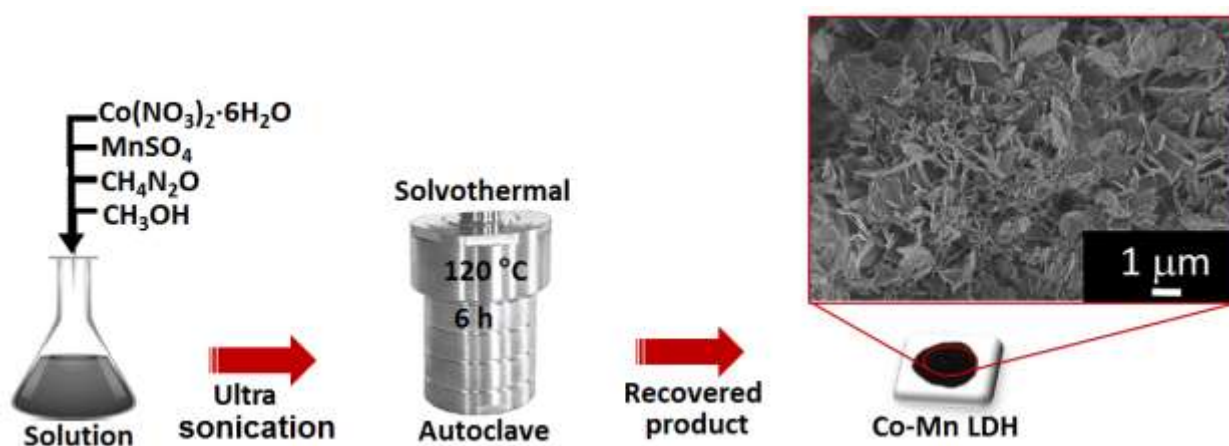
Scheme 1. Schematic of the synthesis route of the Co-Mn LDH nanoflakes (see micrograph image).

Synthesis of AC (Negative electrode material)

Low-cost mesoporous activated carbon was synthesized via a two-step eco-friendly synthesis route (See Scheme 2). Firstly, 10 g of raw cork (Quercus Suber) was properly washed using acetone and deionized water and dried in an oven. Then, the raw cork was put into a 100 ml Teflon lined autoclave which contains 80 ml deionized water and 0.8 ml of 0.5 M sulfuric acid and treated hydrothermally at 160 °C for 12 hours. The addition of sulfuric acid is adopted to reduce the lignin and cellulose content present in the raw cork

material and improve the quality of the hydrochar obtained. The hydrochar produced was then washed severally with distilled water and dried in an oven. The hydrochar was crushed and weighed again followed by activation with potassium hydrogen carbonate ($KHCO_3$) in a 1:1 ratio. Then, the activated hydrochar was put into a quartz tube and carbonized at a ramping temperature of 5 ^{o}C/min from ambient temperature to 850 °C for 2 hours in argon flow. The obtained activated carbon was washed with 3 M HCl (to remove excess unreacted activating agent present and also to wash off any impurities present in the sample) and deionized water and left to dry in the oven at 60 °C for 12 hours.

Scheme 2. Schematic of the synthesis route of the activated carbon.

2.2 Morphological, Structural, Composition and Electrochemical Characterization

Scanning electron microscopy (SEM) analysis was performed using a Zeiss Ultra plus 55 field emission scanning electron microscope (FE-SEM) working at an accelerating voltage of 2.0 kV to determine the morphology of the materials. High resolution transmission electron microscopy (HR-TEM), selected area diffraction (SAED) and the energy-dispersive X-ray (EDX) analysis of the samples were performed using JEOL 2100 (from Tokyo Japan) operated

at 200 kV. X-ray Diffraction (XRD) studies was performed using an XPERT-PRO diffractometer (PANalytical BV the Netherlands) to determine the structural properties of the samples. A Micrometrics TriStar II 3020 analyzer was used to measure the specific surface area (SSA) and pore size distribution (PSD) using the Brunauer-Emmett-Teller (BET) and Barrett-Joyner-Halenda (BJH) techniques. The SSA was obtained from the N_2-adsorption/desorption isotherm while the PSD data was obtained from the desorption part of the BJH isotherm. Fourier transform infrared (FT-IR) spectroscopy was performed in the range of 4000 – 500 cm^{-1} at 2 cm^{-1} resolution using Perkin Elmer Spectrum RX I FT-IR system. Prior to taking the FT-IR measurements, the pellets used were prepared by properly mixing the samples with KBr in a ratio of 100:1. X-ray photoelectron spectroscopy (XPS) measurements of the samples were carried out using a Physical Electronics VersaProbe 5000 spectrometer.

The Co-Mn LDH and AC samples were tested in three- and two-electrode configurations with a multichannel channel Bio-Logic VMP300 potentiostat/galvanostat workstation at room temperature. The AC electrode for the three-electrode measurements was produced by making a homogenous paste of 80 wt % AC material, 15 wt % carbon black (to increase the material conductivity) and 5 wt % polyvinyl difluoride (PVdF) binder with dropwise addition of 1- methyl-2-pyrrolidinone in an agate mortar. The paste was coated on nickel foam current collector and kept in an oven to dry at 60 ^{o}C for 8 hours. The Co-Mn LDH electrode was likewise prepared by making a homogenous paste of 80 wt % Co-Mn LDH material, 10 wt % carbon black, 10 wt % polyvinyl difluoride (PVdF) binder with dropwise addition of 1- methyl-2-pyrrolidinone in an agate mortar and then coated on nickel foam current collector and kept in an oven to dry at 60 ^{o}C for 8 hours. The positive and negative electrodes for the two-electrode measurements were similarly prepared but coated on 16

mm diameter nickel foams and dried in an oven at 60 $^{\circ}$C for 8 hours and was thereafter assembled with a microfiber glass filter paper as separator in a swagelok and 1 M KOH aqueous electrolyte was added to soak the electrodes. The mass loading of the material was 2.88 mg for the negative electrode and 1.92 mg for the positive electrode and total mass of both electrodes was 4.80 mg/cm^2 for the complete cell. In line with the consideration for appropriate mass loading in order to obtain a significant amount of stored energy [45]. The three-electrode measurements were performed in 1 M KOH with glassy carbon as counter electrode and Ag/AgCl as reference electrode. The specific capacitances (C_s) of the Co-Mn-LDH, AC and the Co-Mn LDH//AC hybrid cell electrode which show pseudo-capacitor behavior were evaluated from the integral of discharge curves using equation (1) [42,43]

$$C_s \ (F \ g^{-1}) = \frac{2I}{V^2 m} \int V dt \qquad (1)$$

where I (A) is the current, Δt (s) is the discharge time, V (V) is maximum voltage and m (g) is the total mass of the electrodes. The energy density, E_d and power density, P_d of the electrodes were calculated using equation (2) [43] and (3) [48] respectively;

$$E_d \ (W \ h \ kg^{-1}) = C_s \times V^2/7.2 \qquad (2)$$

$$P_d (W \ kg^{-1}) = E_d/\Delta t \qquad (3)$$

In order to fabricate the hybrid cell, the C_s of the individual electrodes was taken into consideration. This is to ensure a mass balance on the electrode materials such that equal charges exist on the parallel electrodes such that $Q_+ = Q_-$; where Q$_+$ and Q$_-$ is the charge stored on the positive electrode and negative electrodes. The charge Q is expressed as:

$$Q = C_s \, mV \qquad (4)$$

The mass balance is therefore obtained by using the equation:

$$m_+/m_- = C_{S-}V_-/C_{s+}V_+ \qquad\qquad (5)$$

where C_s is the specific capacitance of the electrode material, m is the mass of the electrodes, and *V* is the maximum potential.

The EIS measurements were carried out in open circuit potential in 100 kHz – 10 mHz frequency range to obtain the device behavior at varying frequencies. The device stability tests involved continuously cycling the full device for a large number of cycles and subsequently subjecting it to voltage holding tests and finally a self-discharge test to obtain the device response in practical testing conditions.

3. RESULTS AND DISCUSSION

3.1 Morphological, Structural and Composition Characterization

The SEM micrographs of the Co-Mn LDH and AC samples at low and high magnifications are presented in Fig.1. Figure 1(a) and (b) shows the Co-Mn LDH micrographs with a highly interconnected thin flake-like morphology necessary for interface reactions during electrochemical processes. The Co-Mn LDH nanoflake formation process involves nucleation and growth of the material crystals and is affected by the solvent polarity and solubility [49], hence, the morphology of the material is tuned by the solvent used in the synthesis [49–51].The formation mechanism for the unique flake-like structure of the Co-Mn LDH material is briefly elucidated as follows: The methanol molecules from the solvothermal reaction environment aggregates with an adequate supporting surface for nanoflake growth [38,50,51]. The presence of a mixture of the Co^{2+} and Mn^{2+} ions from the precursor salts

with the Urea also leads to the formation of an initial seed-layer growth template for the self-assembly of the individual crystals necessary for nanoflake growth. The entire process involves a rapid nucleation of individual crystallites, followed by the actual growth and final self-aggregation of the crystallites to form nanosheets [49,52,53]. In the presence of a continuous supply of reacting solvent (methanol) and urea necessary for methanolysis [54] an equilibrium condition is attained between the solid-liquid interfaces. The forces which contribute to the self-aggregation leading to the flake-like morphology includes Van der waal forces, crystal phase interactions, electrostatic and dipolar fields linked with the aggregates [55]. Other newly formed crystallites also align themselves forming initial points of growth for other semi-stable crystallites forming the LDH nanosheets with flake-like morphology [55]. The AC morphology shown in Fig. 1(c) and (d) displays a good interconnected spherical framework consisting mainly of a 3D porous structure. The material framework and morphology shows that the $KHCO_3$ activating agent leads to the production of an activated carbon sample with microspheres suitable for easy and fast diffusion of ions within the material ideal for charge storage consistent with the research findings previously reported [23]. The formation of micro and mesopores in the AC material is as a result of the gasification and evolution of CO_2 and the availability of oxygen in the material. Typically, CO_2 is formed from the breakdown of $KHCO_3$ during the process of activation and is increased during the carbonization process at elevated temperatures. The CO_2 thus, reacts with the intermediate hydrochar which leads to pore formation and enlargement of existing ones. Also, $KHCO_3$ can react with carbon to produce metallic K leading to the production and evolution of CO_2 thus leading to pore formation [27,48].
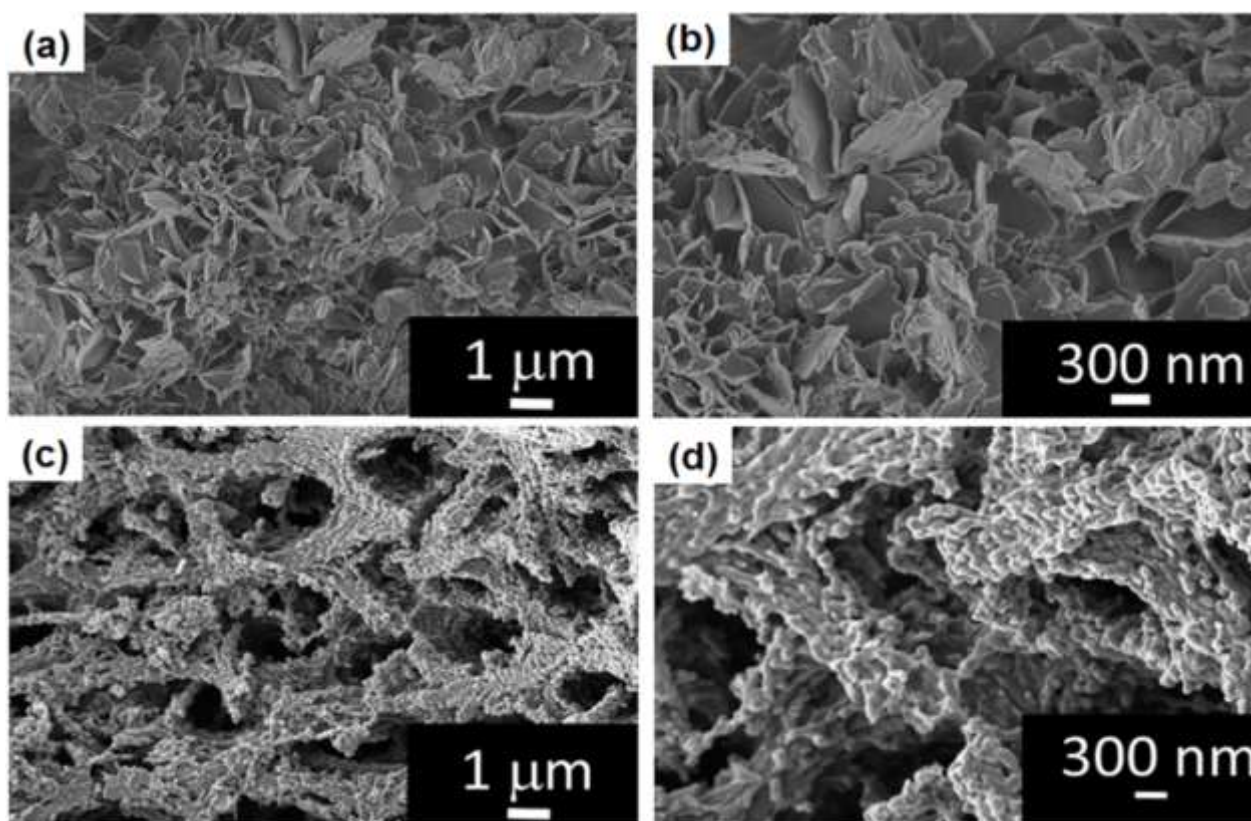
Fig 1. SEM micrographs of Co-Mn LDH nanosheets at (a) low and (b) high magnifications respectively; SEM micrographs of AC porous network at (c) low and (d) high magnifications respectively.

For further information on the morphology, the samples were investigated using HR-TEM. Fig. 2 (a) and (b) shows the HR-TEM micrographs of Co-Mn LDH at low and high magnifications respectively, revealing the nanoflake-like morphology. The inset to Fig. 2 (b) displays a selected area electron diffraction pattern (SAED) of a Co-Mn LDH which shows diffraction rings revealing the polycrystalline nature of the material. In Fig. 2(c), a high magnification HRTEM micrograph of AC is shown which displays no lattice fringes suggesting that AC is not crystalline. Besides, the SAED pattern (inset in Fig. 2(c) does not show diffraction rings revealing that AC is amorphous. EDX analysis was carried out to confirm the elemental composition of the as-prepared Co-Mn LDH and activated carbon materials and is presented in Fig 3 (a) and (b).The EDS spectrum in Fig. 3 (a) confirms the predominance

content of Co and Mn in Co-Mn LDH and the spectrum for activated carbon (Fig. 3 (b)) confirms the predominance content of C in the sample. The observed low-intensity peaks of Si and S could originate from quartz tube or Teflon during sample preparation and the observed Cu (in fig. 3 (a) are due to the formal-coated copper grid.
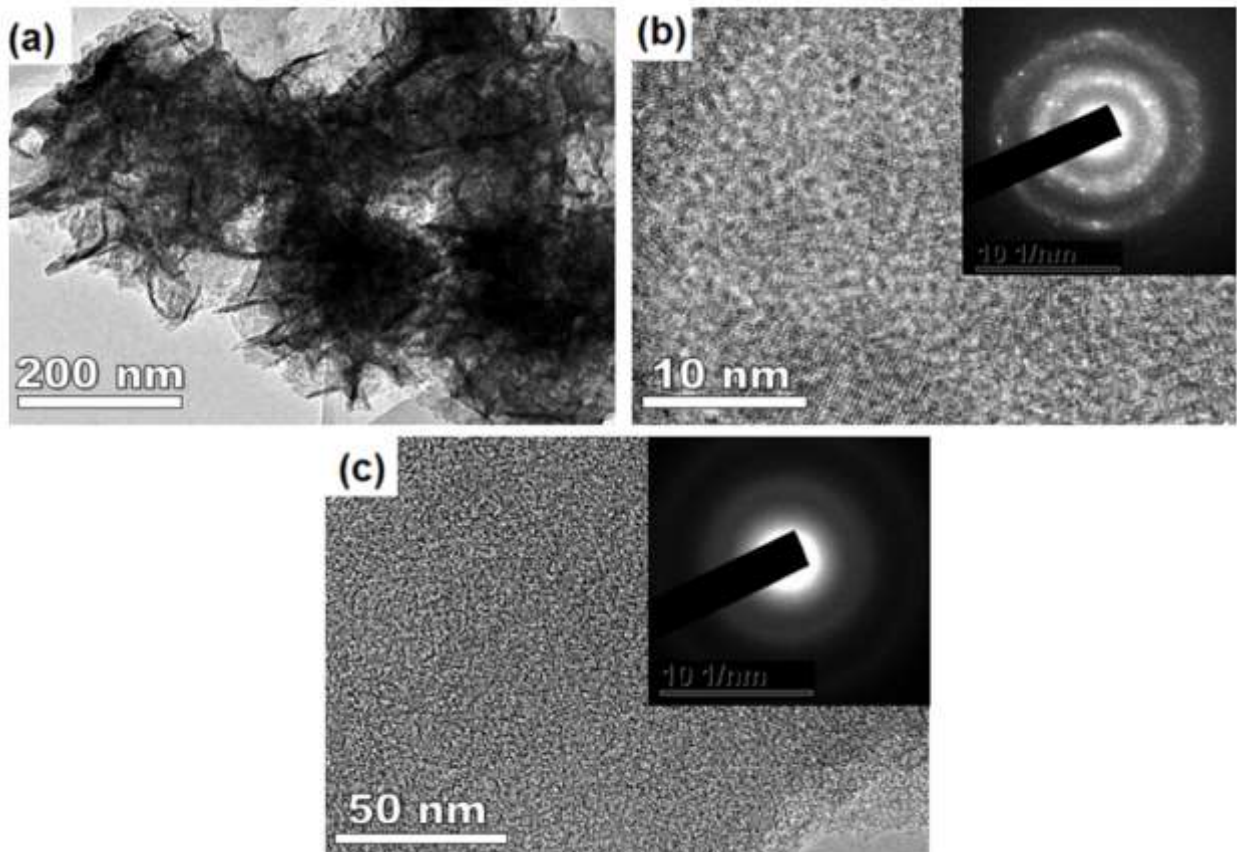

Fig 2. HRTEM micrographs of Co-Mn LDH at (a) low and (b) high magnifications respectively (Inset to (b) is SAED pattern of Co-Mn LDH); (c) HRTEM micrograph of activated carbon and the corresponding SAED pattern (Inset).
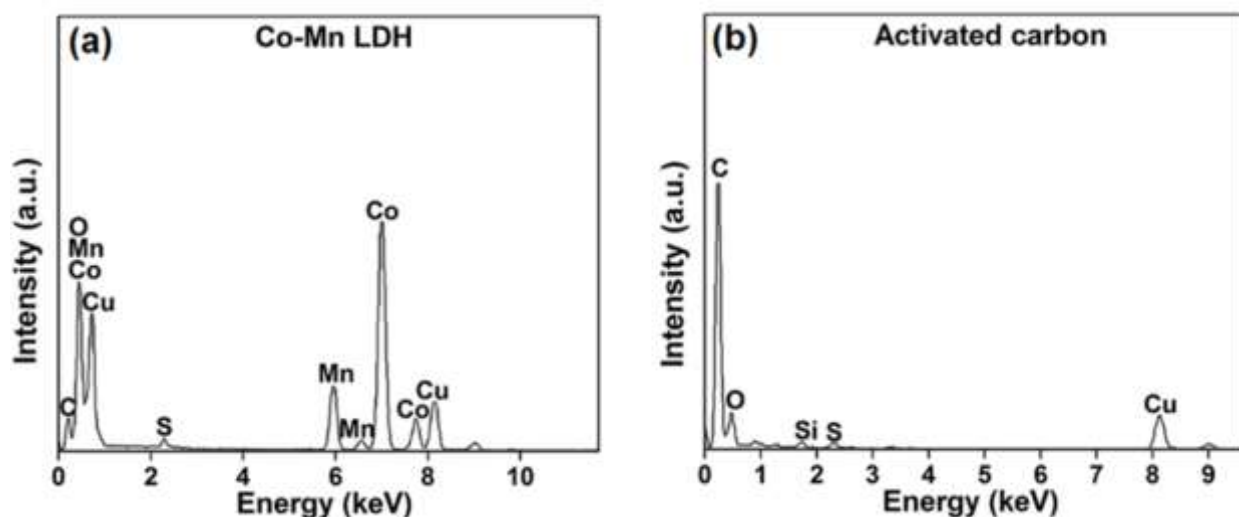
Fig 3. EDS spectra of (a) Co-Mn LDH and (b) Activated carbon.

The structure of the as–synthesized Co-Mn-LDH and AC materials were further investigated by X-ray diffraction using a Co-K$_\alpha$ (1.7890 Å) source. The XRD spectra are presented in Fig. 4 (a) and (b) for the Co-Mn LDH and AC samples respectively. The XRD pattern for the Co-Mn LDH sample (Fig. 4 (a)), showed peaks observed at 2θ values of about 12°, 26°, 39°, 44°, 52°,68° and 70° and corresponding to (003), (006), (009),(015), (018),(110) and (113) lattice planes respectively for a hydrotalcite-like structure of LDH. This is consistent with earlier reports on similar LDH type structures [35,36]. However, the observed peak shifts in positions may be as a result of the Co-K$_\alpha$ X-ray source used for the analysis which is of a different wavelength as compared to Cu-K$_\alpha$ [45]. Fig. 4 (b) reveals the XRD spectrum of the AC sample showing a broad peak at a 2θ angle of 26° and a weak peak at 51° which is related to the (002) and (100) planes of graphitic carbon. The broad and low intensity of the peaks is an indication that the AC material is mostly non-crystalline and therefore can be referred to as amorphous carbon [46]. FT-IR spectrum for the samples performed in the wavenumber range of 4000 - 500 cm^{-1} are presented in Fig. 4 (c) and (d). This measurement is important for the determination of surface functional groups in the as-synthesized Co-Mn

14

LDH and AC samples. the FT-IR spectrum for the Co-Mn LDH (Fig. 4 (a)), shows peaks at ~3440 cm^{-1} and ~1629 cm^{-1} which are due to O-H bending mode of water and hydrogen bonded to the hydroxyl groups [37,47,48]. The peaks appearing at about ~2945 cm^{-1} and ~2815 cm^{-1} and the bands occurring at ~1056 cm^{-1} is related to C – O and C – H stretching vibrations [60]. Whereas the peak position observed at about ~2207 cm^{-1} is due to O-C-O the stretching vibrations of antisymmetric Carbon di-oxide in air [49]. The peak occurring at 1384 cm^{-1} are assigned to the typical vibration of carbonate ions and the peak occurring at about ~627 cm^{-1} is attributed to the metal bonded to the hydroxyl group Co-OH [37,48]. The FT-IR spectra for AC after carbonization at 850 ^{o}C for 2 hours and hydrochar after hydothermal treatment at 160 ^{o}C for 12 hours is presented in Fig. 4 (b). A reduction in the intensity of the peaks of the AC as compared to that of the hydrochar can be observed. This may be due to the breaking of the water molecule bond and loss of moisture in the sample due to carbonization at high temperatures. The ~3435 cm^{-1} is due to the O-H stretching vibrations of water due to surface hydroxyl groups. The bands occurring at ~2942 cm^{-1} in the hydrochar and AC samples indicate the C-H bond of the aliphatic group and the peak at ~1608 cm^{-1} indicates the C = O stretching vibrations of the carboxyl groups. The peaks occurring at ~1180 cm^{-1} and ~502 cm^{-1} may be due to the - C- C stretching vibration [44].

The results from the textural analysis of the samples using the BET measurements are presented in Fig. 5 (a) and (b). The N_2 adsorption-desorption isotherm of the Co-Mn LDH (Fig.. 5 (a)) shows a type III and a H3 hysteresis loop indicating agglomeration of plate-like particles with slit-shaped pores and the presence of mesopores in the double-layered configuration [50]. While the N_2 adsorption-desorption isotherm of the AC sample (see Fig. 5 (b)) shows a type IV and a H4 hysteresis loop demonstrating a composite material comprising of microporous and mesoporous structures. The SSA of the Co-Mn LDH was

recorded as 44.60 m^2 g^{-1} while that of the AC sample was recorded as 1056.52 m^2 g^{-1}. The

insets to Fig. 5 (a) and (b) show the Pore size distribution (PSD) plots for the Co-Mn LDH and

AC samples signifying that the Co-Mn LDH is made up of mainly mesoporous structure with

an overall pore volume of 0.15 cm^3 g^{-1} and average pore diameter of 16.1 nm while the AC is

made up of both micropores and mesopores with overall pore volume of 0.64 cm^3 g^{-1} and

average pore diameter of 3.4 nm. The active micropores and mesopores in the samples

provide the necessary sites for ion trapping required for efficient energy storage and serve

as the channels used for the electrolyte ion transport required for device power delivery
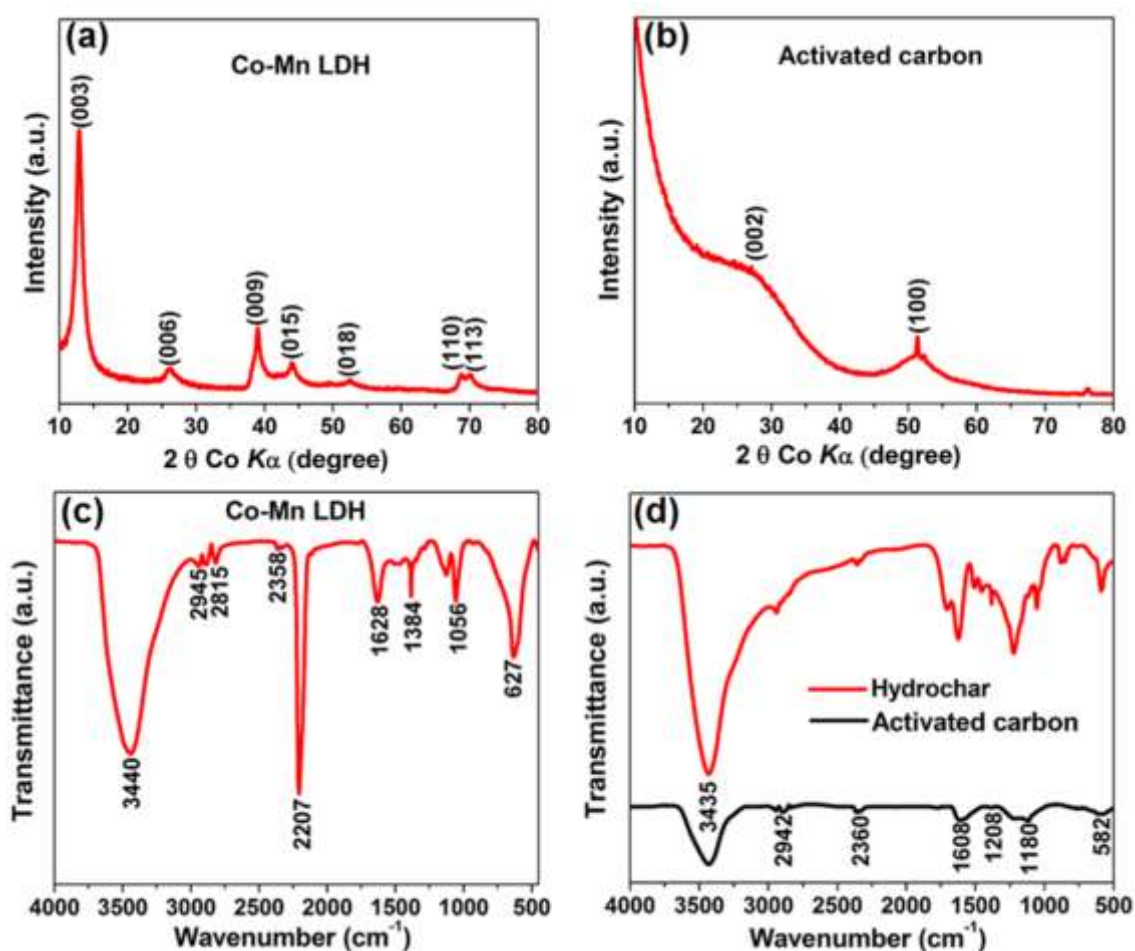
[51].

Fig 4. X-ray diffraction pattern of (a) Co-Mn LDH; and (b) activated carbon; FTIR spectra of (c) Co-Mn LDH and
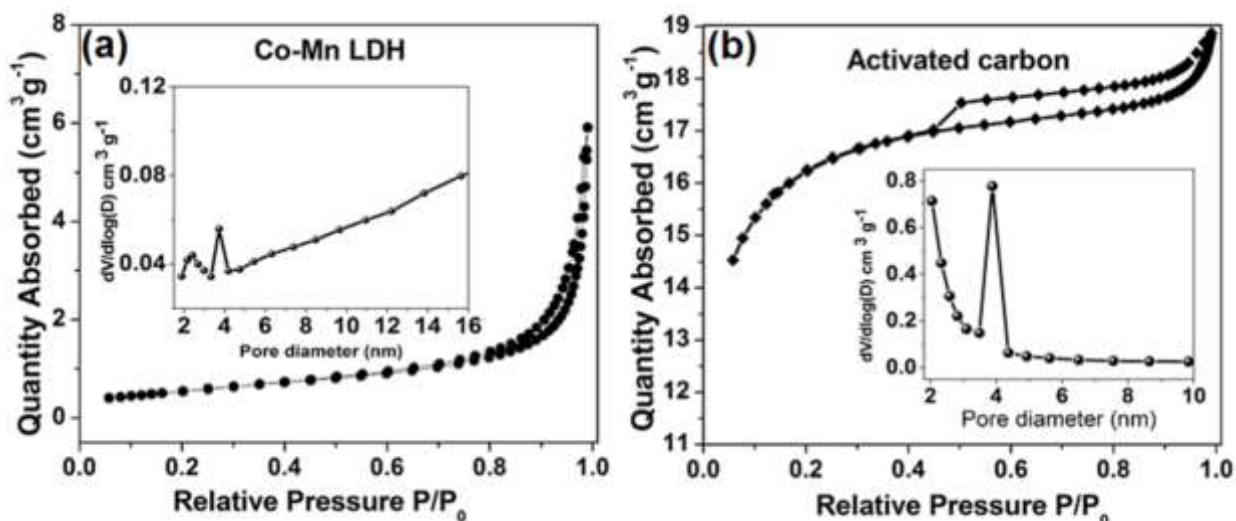
(d) Activated carbon and Hydrochar.

Fig 5. N_2 Adsorption-desorption isotherm for (a) Co-Mn LDH and (b) Activated carbon (Insets to the figure show pore size distribution plots).

Furthermore, to analyze the oxidation states of the Mn and Co in the Co-Mn LDH, the sample was analyzed by XPS including activated carbon sample. Fig. 6(a) shows the wide scan XPS spectra of the as-received Co-Mn LDH sample (i.e. without sputter cleaning) which displays the main elements (Co, Mn, and O) of the composition of the sample. Fig. 6(b) shows the core level spectrum of Co 2p of the Co-Mn LDH sample which reveals the binding energy peaks at 778.4 eV and 783.5 eV which correspond to Co $2p_{3/2}$ core level, and other binding energy peaks at 794.3 eV and 800.9 eV which correspond to Co $2p_{1/2}$ core level. The fitted Co $2p_{3/2}$ peaks suggest that the Co oxidation state of the Co-Mn LDH sample is mainly Co^{2+}. On the other hand, the core level spectrum of Mn 2p of the Co-Mn LDH sample reveals the binding energy peaks at 639.3 and 651.5 eV corresponding to Mn $2p_{3/2}$ and Mn $2p_{1/2}$ core levels, respectively, as shown in Fig. 6 (c). The fitted Mn $2p_{3/2}$ peaks suggest that the Mn oxidation state of the sample is composed of Mn^{2+}, Mn^{3+} and Mn^{4+} [63]. Fig. 6(d) shows the core level spectrum of O 1s with fitted peaks at 528.6 and 529.7 eV which could be
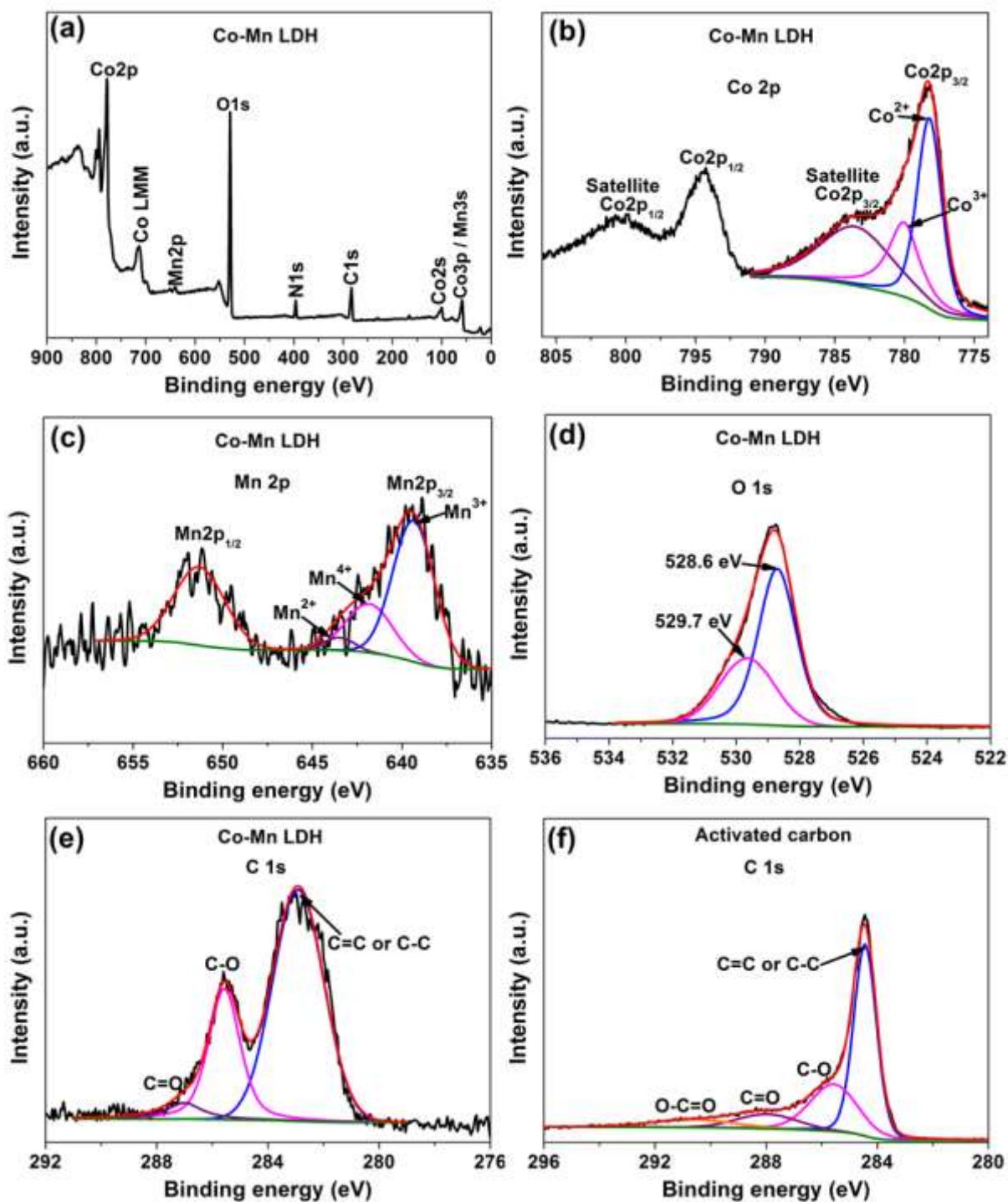
Fig 6: (a) The wide scan XPS spectra of the as-received Co-Mn LDH nanosheets sample. The core level spectrum of (b) Co 2p, (c) Mn 2p, (d) O 1s and (e) C 1s of a Co-Mn LDH nanosheets sample. (f) The core level spectrum of C 1s of an activated carbon.

ascribed to O 1s in Co−O and Mn−O compounds. The core level spectrum of C 1s (Fig. 6 (e)) shows a high-intensity peak at about 283.5 eV which corresponds to the graphitic carbon,

C=C and/or C-C and other fitted peaks related to some of the carbon-oxide components as suggested by FT-IR analysis. Similar to the core level spectrum of C 1s of a Co-Mn LDH sample, the C 1s core level spectrum of the activated carbon sample reveals the graphitic carbon peak (C=C and/or C-C) and carbon-oxides peaks. However, for the activated carbon sample the high-intensity peak at about 284.2 eV (C=C and/or C-C) confirms the predominance content of graphitic carbon in the sample.

3.2 Electrochemical analysis

The results from the electrochemical analysis of Co-Mn LDH positive electrode material and the AC negative electrode material performed in a three electrode configuration is presented in Fig. 7. The CV curves for the Co-Mn LDH positive electrode material performed at scan rates of 10 mV s^{-1} to 100 mVs^{-1} (see Fig. 7 (a)), displayed a very good quasi-reversible faradaic behavior. Two redox couples can be observed with peak separation between 60 to 110 mV for each of the redox peaks, within the negative/positive voltage of -0.2 V to 0.5 V, indicating relatively fast surface redox reactions of the Co^{2+} and Mn^{2+} in the Co-Mn LDH material. The first anodic and cathodic current peaks were observed at ~-0.01 V and ~0.1 V respectively and the second was observed at ~ 0.24 V and 0.39 V respectively. Where the latter is indicative of the quasi-reversible faradaic behavior related to the transition between Co^{2+}/ Co^{3+}at the various scan rates related to the reaction [52,53]

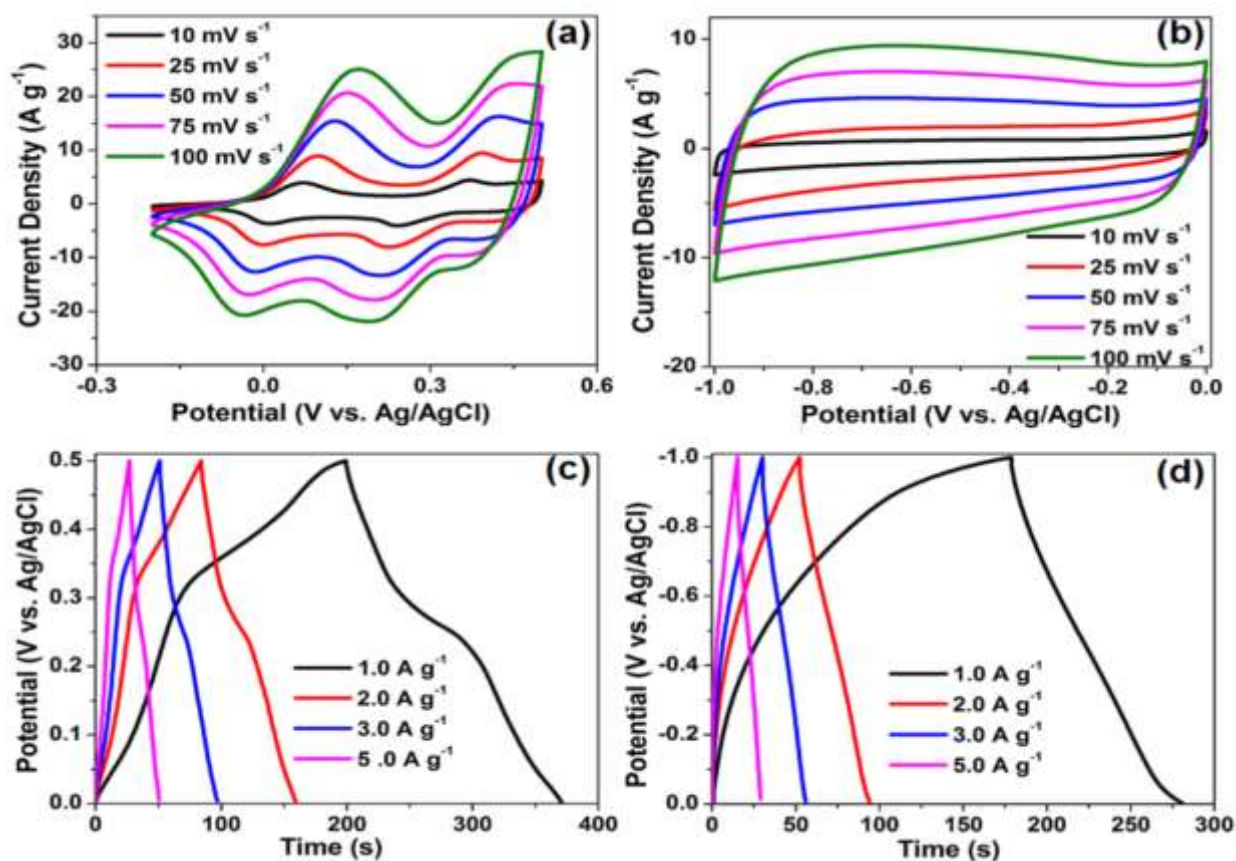$$CoOOH + OH^- \leftrightarrow CoO_2 + H_2O + e \qquad (6)$$

Fig 7. CV curves of (a () Co-Mn LDH from 10 mVs^{-1} to 100 mVs^{-1} (b) AC from 10 mVs^{-1} to 100 mVs^{-1} in 1 M KOH; CD profiles of (c) Co-Mn-LDH and (d) AC at current density of 1.0 A g^{-1} - 5 A g^{-1} in 1 M KOH.

Thus, the first redox couple could be assigned to the reversible faradaic reaction related to transition from Mn^{2+} to Mn^{3+} in the reaction [65] .

$$Mn(OH)_2 + OH^- \leftrightarrow MnOOH + H_2O + e \qquad\qquad (7)$$

The CV curves of the AC material performed at 10 mV s^{-1} - 100 mV s^{-1} scan rates are presented in Fig. 7 (b). The CV curves exhibited rectangular shapes which are related to electric double layer capacitive (EDLC) features for porous carbon materials coupled with a good current response in the negative potential range of -1.0 V – 0.0 V. The results from the charge-discharge (CD) tests performed in the three electrode configuration at varying current densities of 1.0 – 5.0 A g^{-1} for the Co-Mn LDH and AC electrodes are presented in

Fig. 7 (c) and (d). The CD profiles of the Co-Mn LDH and AC electrodes are directly related to the observed redox and EDLC characteristics for the CV curves of the Co-Mn LDH and AC respectively. A specific capacitance of 318 F g^{-1} and 103 F g^{-1} were calculated for the Co-Mn LDH and AC respectively at 1.0 A g^{-1} using equation (1).

The results from testing the assembled hybrid device taking into cognizance the electrochemical performance values obtained from the half-cell analyses of the individual electrodes and adopting the mass balance approach to ensure equal charge concentration is reported in Fig. 8. Figure 8 (a) shows the individual CV curves superimposed to illustrate the combination of the independent operating potentials of both the EDLC and Faradaic-type materials in order to maximize the final operating voltage of the hybrid device. An optimized voltage window was determined by cycling the full device at a moderate 25 mV s^{-1} scan rate whilst varying the voltage from 1.0 V – 1.7 V as shown in Fig. 8 (b). The CV curves mimic the CV shape of AC within the voltage window of 0.0 V – 0.8 V and above 0.8 V that of the LDH seen earlier in Fig. 8 (a). An anodic current leap can be observed beyond 1.6 V which may be attributed to gas evolution as the potential is increased. Therefore, the ideal operating voltage was chosen as 1.5 V for the hybrid device based on the ideality of the CV plot. The hybrid device is able to work within this potential window of 1.5 V, beyond the thermodynamic decomposition of water (1.23 V) in 1 M KOH because of the synergistic operation of the individual operating potentials of the positive electrode and the negative electrode materials, thus, combining the high overpotential for di-hydrogen and oxygen evolutions at the positive and negative electrodes respectively [32,54]. The CV curves of the hybrid device at 5 mV s^{-1} - 100 mV s^{-1} scan rates are presented in Fig. 8 (c). The current response increases as scan rate is increased with the signatory redox peaks still observed from the typical faradaic behavior.
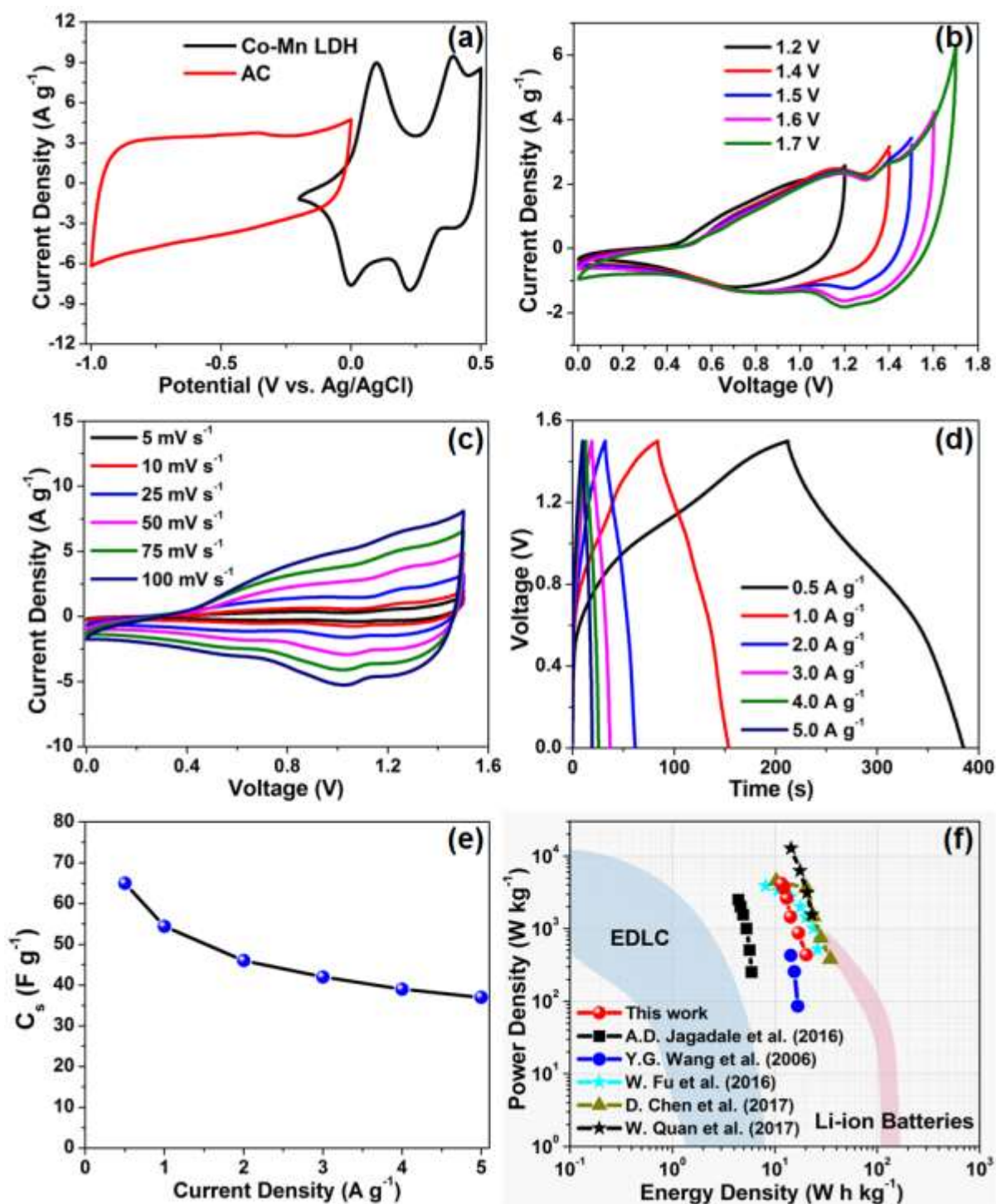
Fig 8. (a) CV curves of AC and Co-Mn LDH at 25 mV s^{-1}, (b) CV plots of hybrid cell of Co-Mn-LDH//AC at 25 mV s^{-1} for different operating voltages in 1 M KOH,(c) CV plots from 5 mV s^{-1} to 100 mV s^{-1}, (d) the associated GCD plots from 0.5 A g^{-1} – 5.0 A g^{-1} in same voltage window, (e) Capacitance variation with current density and (f) Ragone plot.

The associated CD curves of the hybrid cell performed at various current densities are presented in Fig. 8 (d). The calculated specific capacitance value of the Co-Mn LDH//AC hybrid device was recorded as 65 F g^{-1} at 0.5 A g^{-1} current density which decreased to about 37 F g^{-1} (retaining more than 50% of its original value) even when the current density is increased by 10-fold to 5.0 A g^{-1}. This is indicative of good rate capability of the hybrid device as the current is increased. The specific capacitance as a function of current density is presented in Fig. 8 (e). A maximum energy density of 20.3 W h kg^{-1} was recorded for the hybrid device at 0.5 A g^{-1} current density with a corresponding power density of 425 W kg^{-1}. The Ragone plot (Fig. 8 (f)) displays the energy density values as a function of power density, and shows that the energy density values for Co-Mn LDH//AC hybrid device are close to the upper end region of the lithium ion batteries which confirms good EDLC contribution, the dominating faradaic behavior and good electrochemical performance of the of the hybrid device. It is worthy to note that this energy density value is much higher than some earlier reports on similar asymmetric type hybrid devices. For example, CoMn LDH/Ni foam//AC electrodes by A. D. Jagadale et al. [36], CoAl LDH//AC by Y.G. Wang et al. [55], NiMn LDH/MnO_2//AC by W. Quan et al. [68] as shown in Fig. 8 (f). The obtained values in this report are also comparable to other similar research studies reported for $ZnCo_2O_4$@$Ni_xCo_{2x}(OH)_{6x}$//AC by W. Fu et al. [56], $NiCoS_4$@$Co(OH)_2$//AC by R. Li [57] and NiMn LDH/rGO//AC by M. Li [37], CoMn LDH /NF//AC by D. Chen et al. [7]. In addition to the high energy density, the material in this work displays good cycling stability.

The stability response is of utmost importance as it shows the practical electrochemical performance of the device over a period of time and the long term cycling lifespan which are desirable for high performance materials in supercapacitor application [18,58]. The plot of capacitance retention as a function of cycle number performed at 5.0 A g^{-1} current

density is presented in Fig. 9 (a). A steady increase in the capacitance retention of 97.7 % from the 1st cycle to 99.7 % at the 10,000[th] cycle can be observed for the hybrid device. The increase in capacitance retention may be attributed to the accessibility of more pore sites within the active material after several constant GCD cycles. This allows the electrolyte ions to further intercalate and access more pores in the active material thereby improving the electrochemical performance of the hybrid device [59]. Interestingly, the Co-Mn LDH//AC hybrid device displays a superior cycling stability of 99.7 % up to 10,000 constant GCD cycles when compared to other earlier reports such as NiMn LDH/rGO//AC (74.1 % after 10,000 cycles) [37], CoMn LDH/Ni foam//AC (84.2 % after 5000 cycles) [36], $NiCoS_4@Co(OH)_2$//AC (70.10 % after 5000 cycles) [70] , for $ZnCo_2O_4@Ni_xCo_{2x}(OH)_{6x}$//AC (81.4 % after 2000 cycles) [56], $NiMn LDH/MnO_2$//AC (87 % after 5000 cycles) [68] and CoMn LDH /NF//AC (83.7 % after 3000 cycles) [7] (as shown in Fig. 9 (b)). The SEM images of the electrode materials after cycling have been included in the supporting information (Fig. S1) to further validate the stability of the material electrodes. The stability of the device was further tested using the voltage holding method at its maximum operating voltage of 1.6 V and 1.0 A g^{-1} current density for 70 hours and the result is presented in Fig. 9 (c). The voltage holding test (also known as floating test) shows a decrease in the device capacitance after the first 20 hours (approx. 1 day) before stabilizing for the rest of the floating time with a capacitance retention of ~80%. The observed floating performance might be linked to the stable network of the porous carbon structure inhibiting the disintegration or collapse of the material after floating at maximum voltage [44].
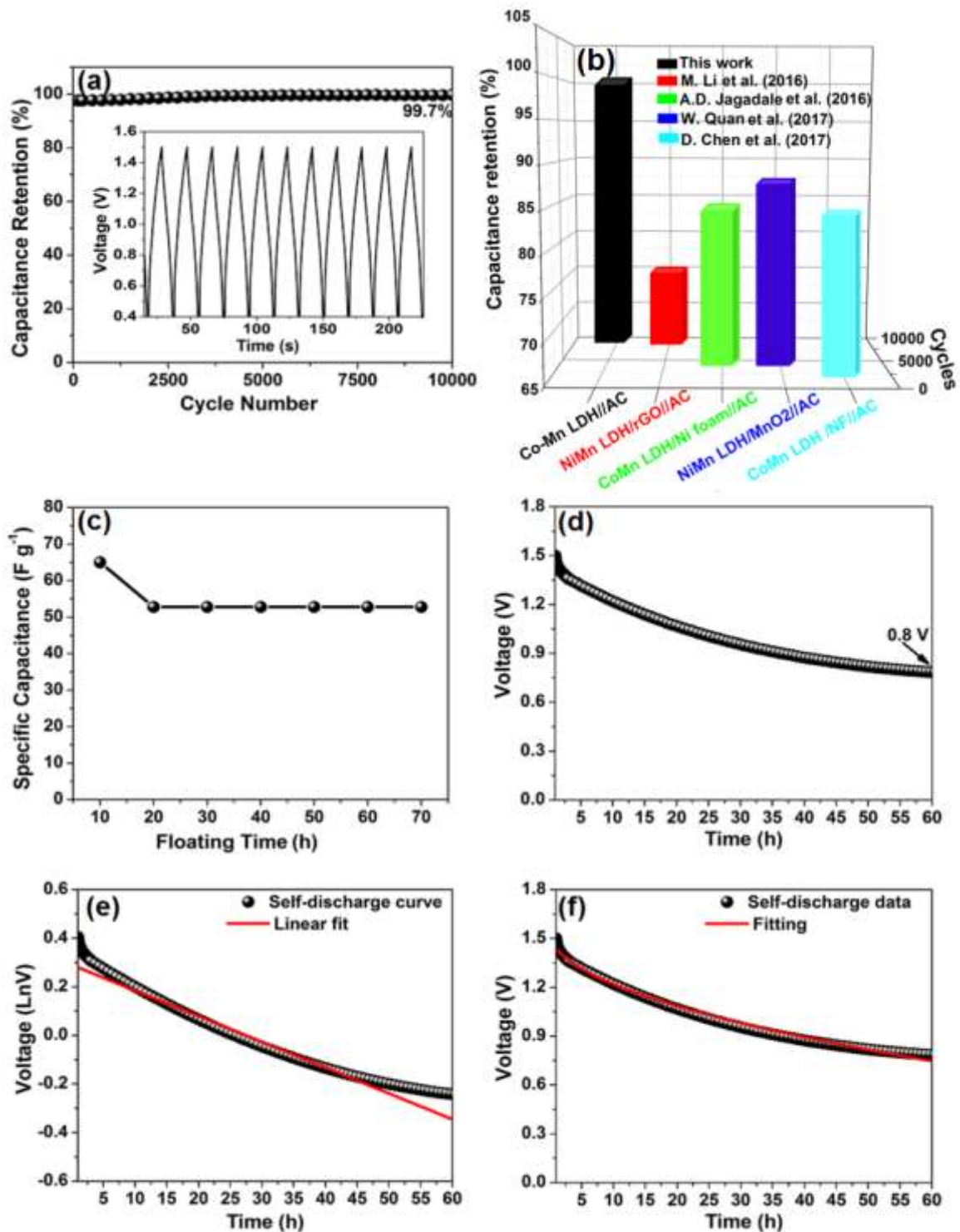
Fig 9. (a) Capacitance retention as a function of cycle number for 10000 continuous charge-discharge cycles; (b) 3D comparison plot of capacitance retention Vs cycle number of the material with previous reports; (c) Plot of Specific capacitance versus voltage holding time after device cycling test, (d) Self-discharge analysis of the hybrid device over a period of 60 h for the Co-Mn-LDH//AC hybrid device, (e) self-discharge with linear fit of the plot of InV as a function of t and (f) self-discharge with polynomial fit from equation 9.

25

Lastly, to conclude all stability tests in relation to practical device operation, the device was subjected to a self-discharge test on open circuit potential to observe the routine device behavior after being fully charged to its maximum operating voltage. The initial drop in the voltage (see Fig. 9 (d)) is attributed to decomposition of any moisture in the electrolyte directly in contact with the active material electrode [60]. As observed in Fig. 9 (d), about 0.8 V is still retained after 60 hours of self-discharge test which means that half of the amount of the initial voltage is retained which shows the potential of the device to retain charge on open potential. The mechanism of self-discharge is described based on the established models in literature [61,62]. The self-discharge can be described by relating the leakage current to a resistance by applying the expression:

$$V = V_0 exp^{(-t/_{RC})} \tag{8}$$

Where V_0 is the maximum applied voltage, R is the resistance and C is the charge stored in the device. The self –discharge curve in this experiment however deviates from the linear fit of the plot of lnV as a function of time (See Fig. 9 (e)). The self-discharge profile subsequently follows a diffusion-controlled process (See Fig. 9 (f)) in which the accumulated ionic-charge are lost during the process of discharge. The discharge profile is governed by the voltage polynomial expressed as:

$$V = V_o - mt^{0.5} \tag{9}$$

where m is a diffusion parameter and is related to V_o, the initial applied maximum voltage and t is the time duration of the self-discharge process.

The EIS study was done in open circuit potential in 10 mHz to 100 kHz frequency range and is presented in Fig.10. Electrochemical impedance spectroscopy (EIS) is very important in

evaluating the electron and ion transport of an electrochemical capacitor [63]. The Nyquist plots for the Co-Mn LDH//AC device before and after stability is presented in Fig. 10 (a). Semicircles in the high frequency regions for the plots before and after stability (inset to the Fig. 10 (a), indicates the presence of charge transfer resistance linked to a resistive element present in the electrode. The nearly vertical lines at the low frequency regions parallel to the y-axis show ideal capacitive behaviors. The intersection of each semicircle with the real Z'-axis shows the solution resistance (R_s) which is a summation of the overall electrolytic resistance, electrode material intrinsic resistance and the resistance between the electrode material and the current collector [46,63]. An R_s-value of 0.46 Ω was recorded for the Nyquist plot before stability, indicating good ion diffusion and conductivity between the electrolyte and the surface of the active material [64]. This might be due to the synergy between the thin nano-flake structure of the Co-Mn LDH and the spherical porous structure of the AC electrodes enabling good electron transport and ion percolation. A value of 0.67 Ω was recorded for the charge transfer resistance (R_{ct}), which is in the Z' – axis intercept from the high to middle frequency region and it is indicative of a good charge transfer and conductivity of the material. The R_s values are smaller than those earlier reported for similar electrode devices such as 0.75 Ω, 0.75 Ω, 0.88 Ω reported for CoMn LDH/Ni foam//AC [36] $ZnCo_2O_4@Ni_xCo_{2x}(OH)_{6x}$//AC [56] and $NiCoS_4@Co(OH)_2$//AC[70] respectively. The R_{ct} value is also smaller than those reported for CoMn LDH/Ni foam//AC (3.4 Ω)[39], $ZnCo_2O_4@Ni_xCo_{2x}(OH)_{6x}$//AC (1.12 Ω) [56] but higher than that reported for $NiCoS_4@Co(OH)_2$//AC(0.01 Ω) [70]. The R_s value recorded after stability is 0.63 Ω which is very close to 0.46 Ω (the Rs value before stability) and the R_{ct} value after stability is 0.68 Ω which is only ~ 1.5 % increase from the value before stability. This shows very good ion

diffusion and conductivity, and low degradation of the material even after 10,000 continuous CD cycles and further confirms the stability of the hybrid device.
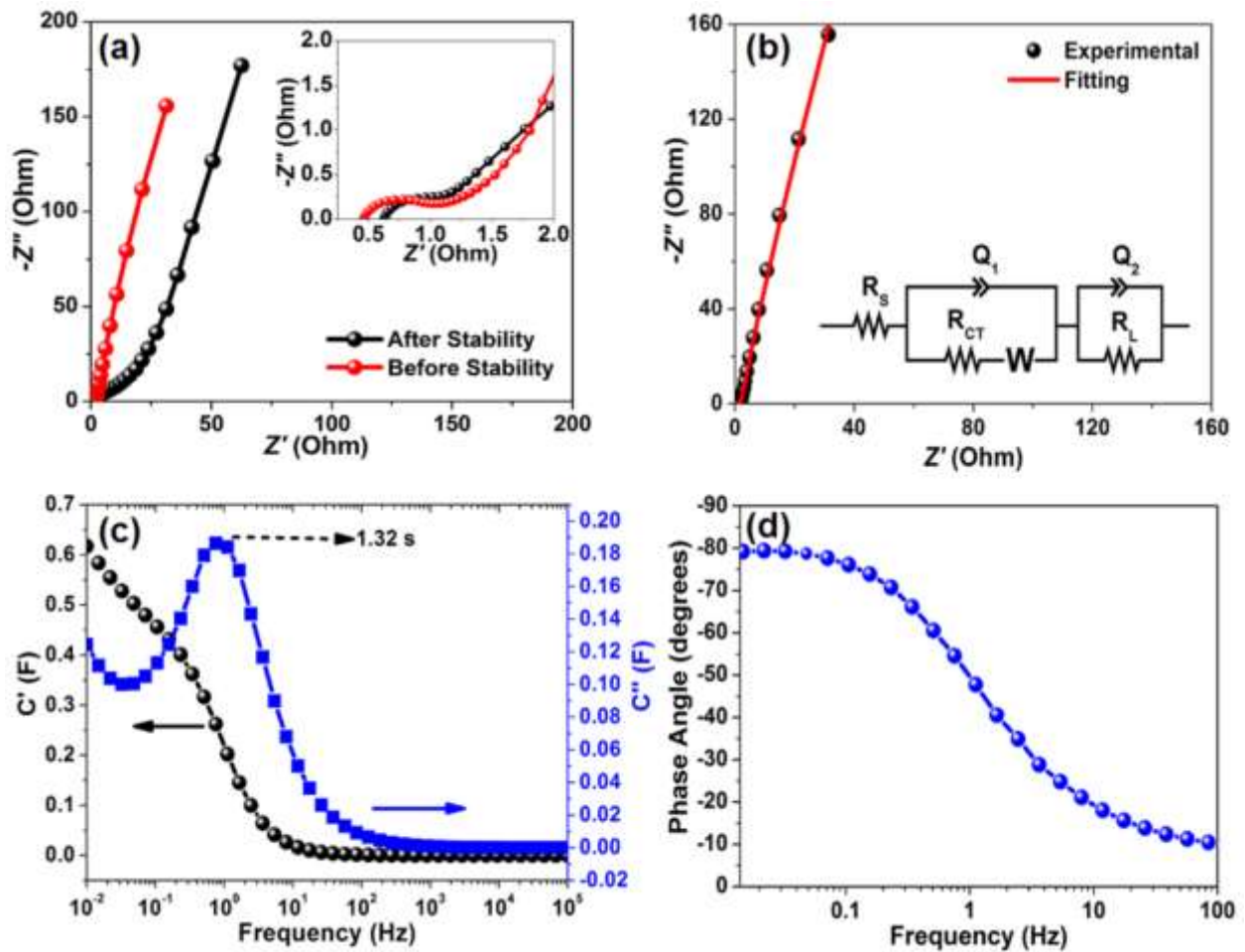

Fig 10. (a) Nyquist plot before and after cycling test; (b) Nyquist plots on open circuit potential with associated equivalent series circuit used for fitting the Nyquist plot data; (c) Real and imaginary part of cell capacitance as a function of frequency and (d) Phase angle as a function of frequency, for the Co-Mn LDH //AC hybrid device in 1M KOH.

The associated equivalent series circuit fitted for the Nyquist plot data is presented in Fig. 10 (b). In the equivalent series circuit (inset to the Fig. 10 (b)), the R_s is in series with Q_1 (constant phase element) which is connected in parallel to the charge transfer resistance R_{ct}. The element, Q_1 is the double layer capacitance attached to the Warburg diffusion element

(W) which is in series with R_{ct}. Q_2 (mass capacitance) is an indication of ideal polarizable capacitance connected in parallel to R_L (impedance element), which is responsible for the deviation of the vertical line from the ideal behavior [34,65]. The shift from the typical vertical behavior also suggests that there is a leakage resistance, R_L which is a resistive element associated with Q_2.

The impedance (Z) of Q_1, is expressed as [34,66];

$$Z_{Q_1} = K(j\omega)^{-b} \tag{10}$$

where ω is angular frequency, k and b are frequency-independent constants. The static or real ($C'(\omega)$) and imaginary($C''(\omega)$) parts of the capacitance as a function of frequency is presented in Fig. 10 (c). From Fig. 10 (d), the capacitance ($C(\omega)$) is the sum of $C'(\omega)$ and $C''(\omega)$ and are expressed by equations (9-11) [67] below:

$$C'(\omega) = -\frac{Z''(\omega)}{\omega|Z(\omega)^2|} \tag{11}$$

$$C''(\omega) = -\frac{Z'(\omega)}{\omega|Z(\omega)^2|} \tag{12}$$

$$C(\omega) = C'(\omega) + jC''(\omega) \tag{13}$$

where $C'(\omega)$ is the static capacitance, $C''(\omega)$ is related to the energy dissipated by the capacitor and also the frequency transition between an ideal capacitive and resistive characteristics [80], ω is the frequency and $|Z(\omega)^2|$ is impedance modulus. The value of C' at a frequency of 10 mHz is 0.63 F which is the real attainable capacitance of the hybrid cell at this frequency. C'' describes the frequency transition between an ideal capacitive and resistive characteristics of the hybrid device [80] with a relaxation time (τ) which was

calculated for the hybrid device as 1.32 s corresponding to a frequency of ~1.0 Hz using the equation:

$$\tau = \frac{1}{f_{max}} = 2\pi\omega_{max}^{-1} \tag{14}$$

The direct interpretation of the relaxation time simply means that the energy stored within the Co-Mn LDH//AC hybrid device can be released in a period of 1.32 s. The plot of phase angle of the cell as a function of frequency is presented in Fig. 10(d). The phase angle is recorded at approximately -80° (close to -90°) which is indicative of the capacitive behavior of the hybrid cell similar to the ideal device.

4. CONCLUSIONS

Thin Co-Mn-LDH nanoflakes with exceptional morphological and textural properties and highly porous activated carbon (AC) from cork raw material (Quercus Suber) and was successfully synthesized by a facile solvothermal and a two-step eco-friendly hydrothermal syntheses routes respectively. A hybrid device was successfully fabricated with a specific capacitance value of 65 F g^{-1} obtained at 0.5 A g^{-1} current density. The device displayed a good rate capability in a 1 M KOH aqueous electrolyte with the energy and power densities of 20.3 Wh kg^{-1} and 425 W kg^{-1} respectively. The device had a remarkable stability response with an initial capacitance retention of 97.7% after a few cycles which subsequently improved to a final capacitance retention value of 99.7% for up to 10,000 constant GCD cycles. There was also negligible degradation recorded after 70 hours of floating time at the maximum cell voltage and the cell still retained more than half of its operating voltage after 60 h of self-discharge test. The results recorded in this study on the Co-Mn LDH//AC hybrid

device depict the as-synthesized material as potential electrodes for high performance supercapacitor applications.

REFERENCES

[1]   J.W. Lee, A.S. Hall, J.-D. Kim, T.E. Mallouk, A Facile and Template-Free Hydrothermal Synthesis of Mn_3O_4 Nanorods on Graphene Sheets for Supercapacitor Electrodes with Long Cycle Stability, Chem. Mater. 24 (2012) 1158–1164. doi:10.1021/cm203697w.

[2]   D.S. Patil, J.S. Shaikh, D.S. Dalavi, S.S. Kalagi, P.S. Patil, Chemical synthesis of highly stable PVA/PANI films for supercapacitor application, Mater. Chem. Phys. 128 (2011) 449–455. doi:10.1016/j.matchemphys.2011.03.029.

[3]   J.K. Gan, Y.S. Lim, A. Pandikumar, N.M. Huang, H.N. Lim, Graphene/polypyrrole-coated carbon nanofiber core–shell architecture electrode for electrochemical capacitors, RSC Adv. 5 (2015) 12692–12699. doi:10.1039/C4RA14922J.

[4]   M.D. Stoller, R.S. Ruoff, Best practice methods for determining an electrode material's performance for ultracapacitors, Energy Environ. Sci. 3 (2010) 1294.

doi:10.1039/c0ee00074d.

[5]   T. Brousse, D. Belanger, J.W. Long, templa, J. Electrochem. Soc. 162 (2015) A5185–

        A5189. doi:10.1149/2.0201505jes.

[6]   X. Zhang, S. Wang, L. Xu, T. He, F. Lu, H. Li, J. Ye, Controllable synthesis of cross-linked

        CoAl-LDH/NiCo 2 S 4 sheets for high performance asymmetric supercapacitors,

        Ceram. Int. (2017). doi:10.1016/j.ceramint.2017.07.159.

[7]   D. Chen, H. Chen, X. Chang, P. Liu, Z. Zhao, J. Zhou, G. Xu, H. Lin, S. Han, Hierarchical

        CoMn-layered double hydroxide nanowires on nickel foam as electrode material for

        high-capacitance supercapacitor, J. Alloys Compd. (2017).

        doi:10.1016/j.jallcom.2017.07.313.

[8]   F. Zhang, T. Zhang, X. Yang, L. Zhang, K. Leng, Y. Huang, Y. Chen, A high-performance

        supercapacitor-battery hybrid energy storage device based on graphene-enhanced

        electrode materials with ultrahigh energy density, Energy Environ. Sci. 6 (2013) 1623.

        doi:10.1039/c3ee40509e.

[9]   K. Grupo Español del Carbón., W. Naoi, Boletin del Grupo Español del Carbón., Grupo

        Español del Carbón, 2005. https://digital.csic.es/handle/10261/81752?locale=en

        (accessed April 8, 2017).

[10]   Z. Fan, J. Yan, T. Wei, L. Zhi, G. Ning, T. Li, F. Wei, Asymmetric Supercapacitors Based

        on Graphene/MnO2 and Activated Carbon Nanofiber Electrodes with High Power and

        Energy Density, Adv. Funct. Mater. 21 (2011) 2366–2375.

        doi:10.1002/adfm.201100058.

[11]   J. Zhao, J. Chen, S. Xu, M. Shao, D. Yan, M. Wei, D.G. Evans, X. Duan, CoMn-layered

        double hydroxide nanowalls supported on carbon fibers for high-performance flexible

        energy storage devices, J. Mater. Chem. A. 1 (2013) 8836. doi:10.1039/c3ta11452j.

[12] C.O. Ania, V. Khomenko, E. Raymundo-Piñero, J.B. Parra, F. Béguin, The Large Electrochemical Capacitance of Microporous Doped Carbon Obtained by Using a Zeolite Template, Adv. Funct. Mater. 17 (2007) 1828–1836. doi:10.1002/adfm.200600961.

[13] C. Portet, Z. Yang, Y. Korenblit, Y. Gogotsi, R. Mokaya, G. Yushin, Electrical Double-Layer Capacitance of Zeolite-Templated Carbon in Organic Electrolyte, J. Electrochem. Soc. 156 (2009) A1-A6. doi:10.1149/1.3002375.

[14] Y. Korenblit, M. Rose, E. Kockrick, L. Borchardt, A. Kvit, S. Kaskel, G. Yushin, High-Rate Electrochemical Capacitors Based on Ordered Mesoporous Silicon Carbide-Derived Carbon, ACS Nano. 4 (2010) 1337-1344. doi:10.1021/nn901825y.

[15] V. Presser, M. Heon, Y. Gogotsi, Carbide-Derived Carbons - From Porous Networks to Nanotubes and Graphene, Adv. Funct. Mater. 21 (2011) 810–833. doi:10.1002/adfm.201002094.

[16] S. Dörfler, I. Felhösi, T. Marek, S. Thieme, H. Althues, L. Nyikos, S. Kaskel, High power supercap electrodes based on vertical aligned carbon nanotubes on aluminum, J. Power Sources. 227 (2013) 218–228. doi:10.1016/j.jpowsour.2012.11.068.

[17] S.R. Sivakkumar, J.M. Ko, D.Y. Kim, B.C. Kim, G.G. Wallace, Performance evaluation of CNT/polypyrrole/MnO2 composite electrodes for electrochemical capacitors, Electrochim. Acta. 52 (2007) 7377–7385. doi:10.1016/j.electacta.2007.06.023.

[18] Q. Gao, L. Demarconnay, E. Raymundo-Piñero, F. Béguin, Exploring the large voltage range of carbon/carbon supercapacitors in aqueous lithium sulfate electrolyte, Energy Environ. Sci. 5 (2012) 9611. doi:10.1039/c2ee22284a.

[19] A. Bello, F. Barzegar, M.J.J. Madito, D.Y.Y. Momodu, A.A.A. Khaleed, T.M.M. Masikhwa, J.K.K. Dangbegnon, N. Manyala, Stability studies of polypyrole- derived

carbon based symmetric supercapacitor via potentiostatic floating test, Electrochim. Acta. 213 (2016) 107–114. doi:10.1016/j.electacta.2016.06.151.

[20]   W. Guo, C. Yu, S. Li, J. Yang, Z. Liu, C. Zhao, H. Huang, M. Zhang, X. Han, Y. Niu, J. Qiu, High-Stacking-Density, Superior-Roughness LDH Bridged with Vertically Aligned Graphene for High-Performance Asymmetric Supercapacitors, Small. (2017) 1701288. doi:10.1002/smll.201701288.

[21]   P. Wang, Y. Li, S. Li, X. Liao, S. Sun, Water-promoted zeolitic imidazolate framework-67 transformation to Ni–Co layered double hydroxide hollow microsphere for supercapacitor electrode material, J. Mater. Sci. Mater. Electron. 28 (2017) 9221–9227. doi:10.1007/s10854-017-6656-5.

[22]   F. Wang, S. Sun, Y. Xu, T. Wang, R. Yu, H. Li, High performance asymmetric supercapacitor based on Cobalt Nickle Iron-layered double hydroxide/carbon nanofibres and activated carbon., Sci. Rep. 7 (2017) 4707. doi:10.1038/s41598-017-04807-1.

[23]   L. Demarconnay, E. Raymundo-Piñero, F. Béguin, Adjustment of electrodes potential window in an asymmetric carbon/MnO2 supercapacitor, J. Power Sources. 196 (2011) 580–586. doi:10.1016/j.jpowsour.2010.06.013.

[24]   W. Gu, G. Yushin, Review of nanostructured carbon materials for electrochemical capacitor applications : advantages and limitations of activated carbon , carbide-derived carbon , aerogels , carbon nanotubes , onion-like carbon , and graphene, WIREs Energy Environ 3(2014)424-473. doi:10.1002/wene.102.

[25]   L.L. Zhang, R. Zhou, X.S. Zhao, Graphene-based materials as supercapacitor electrodes, J. Mater. Chem. 20 (2010) 5983. doi:10.1039/c000417k.

[26]   K. Zhang, L.L. Zhang, X.S. Zhao, J. Wu, Graphene/polyaniline nanofiber composites as

supercapacitor electrodes, Chem. Mater. 22 (2010) 1392–1401.

doi:10.1021/cm902876u.

[27]   M. Sevilla, A.B. Fuertes, A Green Approach to High-Performance Supercapacitor

Electrodes: The Chemical Activation of Hydrochar with Potassium Bicarbonate,

ChemSusChem. 9 (2016) 1880–1888. doi:10.1002/cssc.201600426.

[28]   J. Hayashi, T. Horikawa, I. Takeda, K. Muroyama, F. Nasir Ani, Preparing activated

carbon from various nutshells by chemical activation with K2CO3, Carbon 40 (2002)

2381–2386. doi:10.1016/S0008-6223(02)00118-5.

[29]   A. Jain, C. Xu, S. Jayaraman, R. Balasubramanian, J.Y. Lee, M.P. Srinivasan,

Mesoporous activated carbons with enhanced porosity by optimal hydrothermal pre-

treatment of biomass for supercapacitor applications, Microporous Mesoporous

Mater. 218 (2015) 55–61. doi:10.1016/j.micromeso.2015.06.041.

[30]   A. Jain, R. Balasubramanian, M.P. Srinivasan, Hydrothermal conversion of biomass

waste to activated carbon with high porosity: A review, Chem. Eng. J. 283 (2016) 789–

805. doi:10.1016/j.cej.2015.08.014.

[31]   A. Jain, C. Xu, S. Jayaraman, R. Balasubramanian, J.Y.Y. Lee, M.P.P. Srinivasan,

Mesoporous activated carbons with enhanced porosity by optimal hydrothermal pre-

treatment of biomass for supercapacitor applications, Microporous Mesoporous

Mater. 218 (2015) 55–61. doi:10.1016/j.micromeso.2015.06.041.

[32]   A. Özhan, Ö. Şahin, M.M. Küçük, C. Saka, Preparation and characterization of

activated carbon from pine cone by microwave-induced ZnCl2 activation and its

effects on the adsorption of methylene blue, Cellulose. 21 (2014) 2457–2467.

doi:10.1007/s10570-014-0299-y.

[33]   E. Raymundo-Pinero, P. Azais, T. Cacciaguerra, D. Cazorla-Amorós, a. Linares-Solano,

F. Béguin, E. Raymundo-Piñero, P. Azaïs, T. Cacciaguerra, D. Cazorla-Amorós, a. Linares-Solano, F. Béguin, KOH and NaOH activation mechanisms of multiwalled carbon nanotubes with different structural organisation, Carbon 43 (2005) 786–795. doi:10.1016/j.carbon.2004.11.005.

[34] X. Liu, R. Ma, Y. Bando, T. Sasaki, A General Strategy to Layered Transition-Metal Hydroxide Nanocones: Tuning the Composition for High Electrochemical Performance, Adv. Mater. 24 (2012) 2148–2153. doi:10.1002/adma.201104753.

[35] C. Zhong, Y. Deng, W. Hu, J. Qiao, L. Zhang, J. Zhang, A review of electrolyte materials and compositions for electrochemical supercapacitors, Chem. Soc. Rev. 44 (2015) 7484–7539. doi:10.1039/C5CS00303B.

[36] S.B. Kulkarni, U.M. Patil, I. Shackery, J.S. Sohn, S. Lee, B. Park, S. Jun, High-performance supertcapacitor electrode based on a polyaniline nanofibers / 3D graphene framework as an efficient charge transporter, J.Mater. Chem. A. 2(2014) 4989–4998. doi:10.1039/c3ta14959e.

[37] F. Barzegar, A. Bello, D.Y. Momodu, J.K. Dangbegnon, F. Taghizadeh, M.J. Madito, T. moureen Masikhwa, N. Manyala, J. Madito, T. moureen Masikhwa, N. Manyala, Asymmetric supercapacitor based on an α-MoO3 cathode and porous activated carbon anode materials, RSC Adv. 5 (2015) 37462–37468. doi:10.1039/C5RA03579A.

[38] D. Wang, J. Li, D. Zhang, T. Liu, N. Zhang, Layered Co – Mn hydroxide nanoflakes grown on carbon cloth as binder-free flexible electrodes for supercapacitors, J. Mater. Sci. 51 (2016) 3784–3792. doi:10.1007/s10853-015-9696-3.

[39] A.D. Jagadale, G. Guan, X. Li, X. Du, X. Ma, X. Hao, A. Abudula, Ultrathin nanoflakes of cobalt–manganese layered double hydroxide with high reversibility for asymmetric supercapacitor, J. Power Sources. 306 (2016) 526–534.

doi:10.1016/j.jpowsour.2015.12.097.

[40]   M. Li, J.P. Cheng, J. Wang, F. Liu, X.B. Zhang, The growth of nickel-manganese and cobalt-manganese layered double hydroxides on reduced graphene oxide for supercapacitor, Electrochim. Acta. 206 (2016) 108–115. doi:10.1016/j.electacta.2016.04.084.

[41]   S. Dong, A.Q. Dao, B. Zheng, Z. Tan, C. Fu, H. Liu, F. Xiao, One-step electrochemical synthesis of three-dimensional graphene foam loaded nickel–cobalt hydroxides nanoflakes and its electrochemical properties, Electrochim. Acta. 152 (2015) 195–201. doi:10.1016/j.electacta.2014.09.061.

[42]   H. Chen, L. Hu, M. Chen, Y. Yan, L. Wu, Nickel-Cobalt Layered Double Hydroxide Nanosheets for High-performance Supercapacitor Electrode Materials, Adv. Funct. Mater. 24 (2014) 934–942. doi:10.1002/adfm.201301747.

[43]   L. Zhang, J. Wang, J. Zhu, X. Zhang, K. San Hui, K.N. Hui, 3D porous layered double hydroxides grown on graphene as advanced electrochemical pseudocapacitor materials, J. Mater. Chem. A. 1 (2013) 9046. doi:10.1039/c3ta11755c.

[44]   L.-H.H. Su, X.-G.G. Zhang, Y. Liu, Electrochemical performance of Co-Al layered double hydroxide nanosheets mixed with multiwall carbon nanotubes, J. Solid State Electrochem. 12 (2008) 1129–1134. doi:10.1007/s10008-007-0455-5.

[45]   A. Balducci, D. Belanger, T. Brousse, J.W. Long, W. Sugimoto, Perspective—A Guideline for Reporting Performance Metrics with Electrochemical Capacitors: From Electrode Materials to Full Devices, J. Electrochem. Soc. 164 (2017) A1487–A1488. doi:10.1149/2.0851707jes.

[46]   B. Akinwolemiwa, C. Peng, G.Z. Chen, Redox Electrolytes in Supercapacitors, J. Electrochem. Soc. 162 (2015) A5054–A5059. doi:10.1149/2.0111505jes.

[47] A. Laheaar, P. Przygocki, Q. Abbas, F. B??guin, A. Laheäär, P. Przygocki, Q. Abbas, F. Béguin, Appropriate methods for evaluating the efficiency and capacitive behavior of different types of supercapacitors, Electrochem. Commun. 60 (2015) 21–25. doi:10.1016/j.elecom.2015.07.022.

[48] A. Bello, N. Manyala, F. Barzegar, A.A. Khaleed, D.Y. Momodu, J.K. Dangbegnon, Renewable pine cone biomass derived carbon materials for supercapacitor application, RSC Adv. 6 (2016) 1800–1809. doi:10.1039/C5RA21708C.

[49] Y. Song, J. Wang, Z. Li, D. Guan, T. Mann, Q. Liu, M. Zhang, L. Liu, Self-assembled hierarchical porous layered double hydroxides by solvothermal method and their application for capacitors, Microporous Mesoporous Mater. 148 (2012) 159–165. doi:10.1016/j.micromeso.2011.08.013.

[50] F. Deng, L. Yu, M. Sun, T. Lin, G. Cheng, B. Lan, F. Ye, Controllable Growth of Hierarchical NiCo2O4 Nanowires and Nanosheets on Carbon Fiber Paper and their Morphology-Dependent Pseudocapacitive Performances, Electrochim. Acta. 133 (2014) 382–390. doi:10.1016/j.electacta.2014.04.070.

[51] L. Yu, L. Zhang, H. Bin Wu, G. Zhang, X.W. (David) Lou, Controlled synthesis of hierarchical $Co_x Mn_{3-x} O_4$ array micro-/nanostructures with tunable morphology and composition as integrated electrodes for lithium-ion batteries, Energy Environ. Sci. 6 (2013) 2664–2671. doi:10.1039/C3EE41181H.

[52] S. Liu, S.C. Lee, U. Patil, I. Shackery, S. Kang, K. Zhang, J.H. Park, K.Y. Chung, S. Chan Jun, Hierarchical MnCo-layered double hydroxides@Ni(OH)$_2$ core–shell heterostructures as advanced electrodes for supercapacitors, J. Mater. Chem. A. 5 (2017) 1043–1049. doi:10.1039/C6TA07842G.

[53] G.H. and, D. O'Hare, Unique Layered Double Hydroxide Morphologies Using Reverse

Microemulsion Synthesis, J.AM.Chem.Soc. 127 (2005) 17808-17813.

doi:10.1021/JA0549392.

[54] K. Shukla, V.C. Srivastava, Synthesis of organic carbonates from alcoholysis of urea: A review, Catal. Rev. 59 (2017) 1–43. doi:10.1080/01614940.2016.1263088.

[55] L. Xu, Y.-S. Ding, C.-H. Chen, L. Zhao, C. Rimkus, R. Joesten, S.L. Suib, 3D Flowerlike α-Nickel Hydroxide with Enhanced Electrochemical Activity Synthesized by Microwave-Assisted Hydrothermal Method, Chem. Mater. 20 (2008) 308–316. doi:10.1021/cm702207w.

[56] D. Momodu, A. Bello, J. Dangbegnon, F. Barzeger, F. Taghizadeh, M. Fabiane, A.T.C. Johnson, N. Manyala, Solvothermal synthesis of NiAl double hydroxide microspheres on a nickel foam-graphene as an electrode material for pseudo-capacitors, AIP Adv. 4 (2014) 097122. doi:10.1063/1.4896125.

[57] N. Manyala, A. Bello, F. Barzegar, A.A.A. Khaleed, D.Y.Y. Momodu, J.K.K. Dangbegnon, Coniferous pine biomass: A novel insight into sustainable carbon materials for supercapacitors electrode, Mater. Chem. Phys. 182 (2015) 139–147. doi:10.1016/j.matchemphys.2016.07.015.

[58] A.N. Naveen, S. Selladurai, A 1-D/2-D hybrid nanostructured manganese cobaltite–graphene nanocomposite for electrochemical energy storage, RSC Adv. 5 (2015) 65139–65152. doi:10.1039/C5RA09288D.

[59] J.P. Cheng, L. Liu, J. Zhang, F. Liu, X.B. Zhang, Influences of anion exchange and phase transformation on the supercapacitive properties of α-Co(OH)2, J. Electroanal. Chem. 722–723 (2014) 23–31. doi:10.1016/j.jelechem.2014.03.019.

[60] B.K. Pandey, A.K. Shahi, R. Gopal, Magnetic colloid by PLA: Optical, magnetic and thermal transport properties, Appl. Surf. Sci. 347 (2015) 461–470.

doi:10.1016/j.apsusc.2015.04.045.

[61]   W. Yang, Z. Gao, J. Wang, J. Ma, M. Zhang, L. Liu, Solvothermal one-step synthesis of Ni-Al layered double hydroxide/carbon nanotube/reduced graphene oxide sheet ternary nanocomposite with ultrahigh capacitance for supercapacitors., ACS Appl. Mater. Interfaces. 5 (2013) 5443–5454.doi:10.1021/am4003843.

[62]   M. Zhi, C. Xiang, J. Li, M. Li, N. Wu, Nanostructured carbon-metal oxide composite electrodes for supercapacitors: a review., Nanoscale. 5 (2013) 72–88. doi:10.1039/c2nr32040a.

[63]   S. Hu, Y. Li, F. Lai, X. Zhang, Q. Li, Y. Huang, X. Yuan, J. Chen, H. Wang, Enhanced electrochemical performance of $LiMn_2O_4$ cathode with a $Li_{0.34}La_{0.51}TiO_3$-coated layer, RSC Adv. 5 (2015) 17592–17600. doi:10.1039/C4RA15374J.

[64]   C. Guan, J. Liu, C. Cheng, H. Li, X. Li, W. Zhou, H. Zhang, H.J. Fan, Hybrid structure of cobalt monoxide nanowire @ nickel hydroxidenitrate nanoflake aligned on nickel foam for high-rate supercapacitor, Energy Environ. Sci. 4 (2011) 4496. doi:10.1039/c1ee01685g.

[65]   S.I. Cordoba, R.E. Carbonio, M.L. Teijelo, V.A. Macagno, The electrochemical response of binary mixtures of hydrous transition metal hydroxides co-precipitated on conducting substrates with reference to the oxygen evolution reaction, Electrochim. Acta. 31 (1986) 1321–1332. doi:10.1016/0013-4686(86)80155-4.

[66]   K. Fic, G. Lota, M. Meller, E. Frackowiak, Novel insight into neutral medium as electrolyte for high-voltage supercapacitors, Energy Environ. Sci. 5 (2012) 5842–5850. doi:10.1039/C1EE02262H.

[67]   Y.-G. Wang, L. Cheng, Y.-Y. Xia, Electrochemical profile of nano-particle CoAl double hydroxide/active carbon supercapacitor using KOH electrolyte solution, J. Power

Sources. 153 (2006) 191–196. doi:10.1016/j.jpowsour.2005.04.009.

[68]   W. Quan, C. Jiang, S. Wang, Y. Li, Z. Zhang, Z. Tang, F. Favier, New nanocomposite

material as supercapacitor electrode prepared via restacking of Ni-Mn LDH and MnO

2 nanosheets, Electrochim. Acta. 247 (2017) 1072–1079.

doi:10.1016/j.electacta.2017.07.010.

[69]   W. Fu, Y. Wang, W. Han, Z. Zhang, H. Zha, E. Xie, Construction of hierarchical $ZnCo_2O_4$ @$Ni_xCo_{2x}(OH)_{6x}$ core/shell nanowire arrays for high-performance supercapacitors,

J. Mater. Chem. A. 4 (2016) 173–182. doi:10.1039/C5TA07965A.

[70]   R. Li, S. Wang, Z. Huang, F. Lu, T. He, NiCo2S4@Co(OH)2 core-shell nanotube arrays in

situ grown on Ni foam for high performances asymmetric supercapacitors, J. Power

Sources. 312 (2016) 156–164. doi:10.1016/j.jpowsour.2016.02.047.

[71]   V. Ruiz, R. Santamaría, M. Granda, C. Blanco, Long-term cycling of carbon-based

supercapacitors in aqueous media, Electrochim. Acta. 54 (2009) 4481–4486.

doi:10.1016/j.electacta.2009.03.024.

[72]   G. Ren, X. Pan, S. Bayne, Z. Fan, Kilohertz ultrafast electrochemical supercapacitors

based on perpendicularly-oriented graphene grown inside of nickel foam, Carbon 71

(2014) 94–101. doi:10.1016/j.carbon.2014.01.017.

[73]   L. Chen, H. Bai, Z. Huang, L. Li, J. Zhang, L. Zhang, A. Pirkle, R.M. Wallace, K.A. Cychosz,

M. Thommes, D. Su, E.A. Stach, R.S. Ruoff, Mechanism investigation and suppression

of self-discharge in active electrolyte enhanced supercapacitors, Energy Environ. Sci.

7 (2014) 1750–1759. doi:10.1039/C4EE00002A.

[74]   A.A. Khaleed, F.U. Ugbo, K.O. Oyeniran, D.Y. Momodu, A. Bello, J.K. Dangbegnon, N.

Manyala, Cycling and floating performance of symmetric supercapacitor derived from

coconut shell biomass, AIP Advances 6 (2016)115306. doi:10.1063/1.4967348.

[75]   E.C.S. Transactions, T.E. Society, Floating of PPY Derived Carbon Based Symmetric

       Supercapacitor in Alkaline Electrolyte, ECS Trans. 6 (2017) 3–5.

[76]   J. Luo, H.D. Jang, J. Huang, Effect of Sheet Morphology on the Scalability of Graphene-

       Based Ultracapacitors, ACS Nano. 7 (2013) 1464–1471. doi:10.1021/nn3052378.

[77]   B. Abdulhakeem, B. Farshad, M. Damilola, T. Fatemeh, F. Mopeli, D. Julien, M. Ncholu,

       Morphological characterization and impedance spectroscopy study of porous 3D

       carbons based on graphene foam-PVA/phenol-formaldehyde resin composite as an

       electrode material for supercapacitors, RSC Adv. 4 (2014) 39066.

       doi:10.1039/C4RA05425C.

[78]   H. Wang, Y. Liang, T. Mirfakhrai, Z. Chen, H. Sanchez Casalongue, H. Dai, Advanced

       Asymmetrical Supercapacitors Based on Graphene Hybrid Materials, Nano Res. 4

       (2011)729-736. doi:10.1007/s1227-011-0129-6

[79]   D. Pech, M. Brunet, H. Durou, P. Huang, V. Mochalin, Y. Gogotsi, P.-L. Taberna, P.

       Simon, Ultrahigh-power micrometre-sized supercapacitors based on onion-like

       carbon, Nat. Nanotechnol. 5 (2010) 651–654. doi:10.1038/nnano.2010.162.

[80]   P.L. Taberna, P. Simon, J.F. Fauvarque, Electrochemical Characteristics and Impedance

       Spectroscopy Studies of Carbon-Carbon Supercapacitors, J. Electrochem. Soc. 150

       (2003) A292. doi:10.1149/1.1543948.

The SEM micrographs of the Co-Mn LDH and AC electrode materials after cycling at low and high magnifications are presented in Fig S1. Figure S1 (a) and (b) show the Co-Mn LDH micrographs with highly interconnected thin nanoflake-like morphology. From the Co-Mn LDH electrode material SEM images, well-defined and smoother hexagonal nanoflake-like structure can be observed, suggesting that the integrity of Co-Mn LDH is preserved after cycling. The AC electrode material presented in Fig S1 (c) and (d) shows an interconnected spherical porous network of the material. A more dispersed arrangement of the microspheres in network structure can be observed in the SEM image as compared to the SEM image before electrochemical testing and cycling (Fig. 1 (c) and (d)). The dispersed structural network might be attributed to a breakdown of the initial structure as a result of the effect of sample preparation process and cycling. However, the microspheres structure retained by the material is an indication of the good structural stability of the sample.
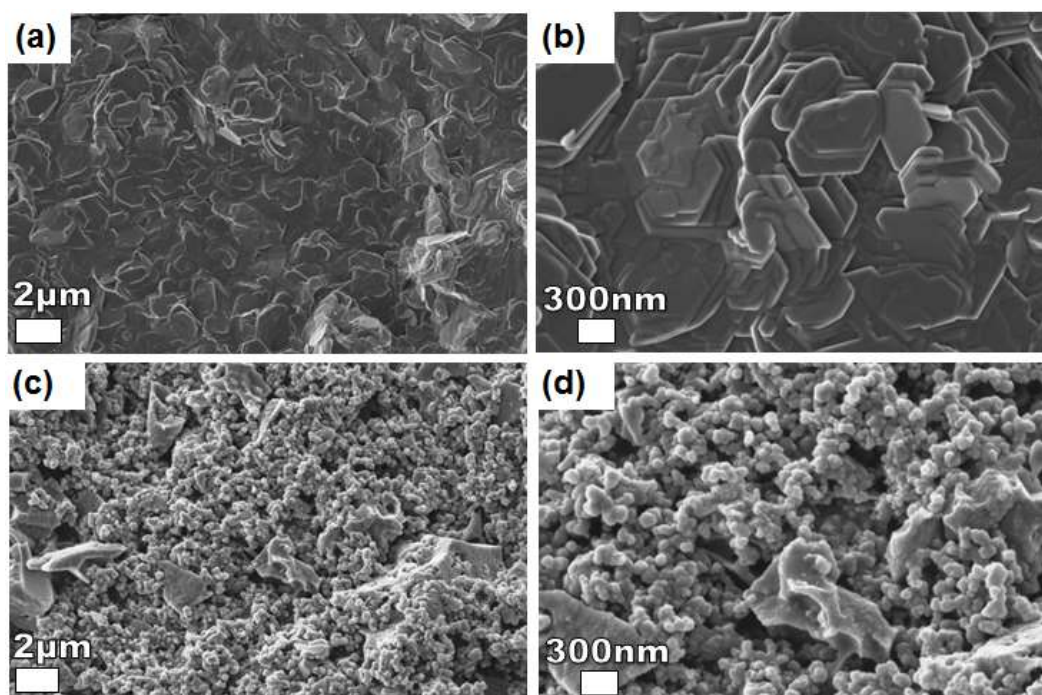

Fig S1. SEM micrographs showing the Co-Mn layered double hydroxide nanosheets electrode materials after cycling at (a) low magnification and (b) high magnification; Activated carbon porous electrode materials after cycling at (c) low magnification and (d) high magnification.